




# Microstructural Evolution of Steel During Magnetic Field-Assisted Processing

M.E. HURLEY<sup>1,6</sup> , R.K. BOLLINENI,<sup>2</sup> A.M. DONALD,<sup>3,4</sup>  
S. FLYNN,<sup>3,4</sup> J.J. HAMLIN,<sup>3</sup> M.S. KESLER,<sup>5</sup> M.V. MANUEL,<sup>1</sup>  
M.W. MEISEL,<sup>3,4</sup> L. LI,<sup>2</sup> and V.M. MILLER<sup>1</sup>

1.—Department of Materials Science and Engineering, University of Florida, Gainesville, FL 32611, USA. 2.—Department of Mechanical Engineering, Virginia Tech, Blacksburg, VA 24061, USA. 3.—Department of Physics, University of Florida, Gainesville, FL 32611-8440, USA. 4.—National High Magnetic Field Laboratory, Gainesville, FL 32611-8440, USA. 5.—Oak Ridge National Laboratory, Oak Ridge, TN 37830, USA. 6.—e-mail: megan.hurley@ufl.edu

Advancing magnetic field-assisted processing, as an energy-efficient method for tailoring steel microstructures, requires a thorough understanding of how the high magnetic field impacts microstructural evolution, particularly its effect on prior austenite grain structures. The current investigation of a near-eutectoid composition, Fe-C alloy, uses electron backscatter diffraction to examine the morphology and orientation of martensite and pearlite microstructures, and to reconstruct the parent austenite microstructures present during equivalent heating under varied magnetic field strengths (0-T, 2-T, 5-T, and 9-T). It was observed that the magnetic field has a negligible effect on martensite lath/block width, slightly decreases prior austenite grain size, and increases the fraction of austenite grains with annealing twins. Additionally, the magnetic field increases the phase fraction of proeutectoid ferrite but has a negligible effect on pearlite block size and the distribution of boundary misorientation angles. No preferred texture was induced by the magnetic field, regardless of the applied field direction, in the proeutectoid ferrite phase or the martensite and prior austenite microstructures. The observed results contradict previous literature, and the differences are discussed.

## INTRODUCTION

Magnetic field-assisted processing is a promising technology in steel manufacturing because it has shown potential to shorten heat treatment times, thereby reducing the total energy input required. It has also been demonstrated to have the ability to produce unique microstructures that have not been obtainable by other means.<sup>1</sup> However, some aspects of the magnetic field effects, especially on the prior austenite structure, have not been systematically studied.

In the Fe-C system, the impacts of a high magnetic field on microstructure primarily result from a shift of the eutectoid invariant reaction to higher temperatures and carbon contents.<sup>2–5</sup> As a result of this shift in phase equilibria, increases in proeutectoid ferrite phase fractions with increasing field strength are commonly observed for hypoeutectoid and near-eutectoid compositions.<sup>4,6–8</sup> Relatedly, decreases in proeutectoid cementite are observed in hypereutectoid compositions.<sup>9</sup> This thermodynamic shift with changing field strength results in different driving forces for nucleation during equivalent cooling, resulting in apparent kinetic differences.<sup>4,10</sup> Increasing field strength has also been shown to increase the martensite start temperature ( $M_S$ ) and bainitic transformation temperature in both Fe-C<sup>11–15</sup> and other alloy<sup>16–18</sup>

(Received October 15, 2024; accepted January 29, 2025;  
published online February 26, 2025)

systems. The increase in  $M_s$  promotes martensite formation, resulting in a reduced volume fraction of retained austenite.<sup>16,19</sup>

In addition to shifts in phase transition temperatures, processing in high magnetic fields has been reported to alter the microstructural morphology resulting from austenite decomposition. In hypoeutectoid steels, it has been frequently observed that the ferrite grains align and elongate along the field direction.<sup>8,9,20–24</sup> Similarly, when martensite was heated above the austenitizing temperature, the resultant austenite grains demonstrated elongation along the field direction.<sup>25</sup> No alignment was reported in hypereutectoid steels.<sup>9</sup> Additionally, it has been reported that, in hypoeutectoid steels, the formation of Widmanstätten ferrite is suppressed in favor of a blockier or idiomorphic morphology. Most works have reported that there is no texture in either the ferrite or pearlite grains formed upon cooling in a magnetic field;<sup>7,8,21,22</sup> however, one report suggested that  $\langle 001 \rangle$  directions align with the transverse field direction.<sup>26</sup> This contradiction requires additional investigation.

The role of magnetic field-assisted processing in developing morphologies of martensitic microstructures is substantially less investigated. Several investigators have examined magnetic field effects on thermal martensites<sup>12,17,18,27</sup> and found that a field can cause morphological differences and promote certain orientations. To the authors' knowledge, there has not been a prior study of athermal martensite morphologies developed in magnetic fields.

One of the largest gaps in understanding the development of carbon steel microstructures under a magnetic field is the evolution of the prior austenite structure. A thorough understanding of the austenite structure is crucial because it dictates the resulting transformation microstructures.<sup>15,28,29</sup> The most relevant study was conducted by Li and Liu,<sup>10</sup> who examined the role of a magnetic field in austenite formation during heating in a hypereutectoid steel. They found that the presence of the field decreases the nucleation rate of austenite during heating, but did not affect the later coarsening rate. The orientation of the specimens relative to the field direction was not reported, and the prior austenite grain size distributions were not quantified.

The goal of the present study is to characterize the microstructural morphologies that result from magnetic field-assisted processing of an Fe-C alloy with near-eutectoid composition, with particular emphasis on the role of the prior austenite grain structure. Recent advances in electron backscatter diffraction (EBSD) detector speeds and parent grain reconstruction techniques<sup>30,31</sup> offer new opportunities to study the prior austenite structure developed under field and its role in the final pearlitic and martensitic microstructures.

## EXPERIMENTAL METHODOLOGY

Two specimen geometries were obtained from a homogenized cast ingot of a binary Fe-C alloy with a carbon composition of 0.63 wt%, which was found by an outside commercial laboratory using LECO analysis. Cylindrical rods were extracted by wire electrical discharge machining (EDM) before being sectioned to approximately 5 mm in diameter and 7 mm in height using a low-speed saw. Rectangular specimens with dimensions of 10 mm in thickness, 10 mm in width, and 50 mm in length were also extracted by wire EDM.

The University of Florida's High BxT facility and Oak Ridge National Laboratory (ORNL) are both equipped with different thermomagnetic processing systems (TMP). The UF TMP system uses a resistive furnace, which operates within a home-made chilled-water jacket insert found in the 90-mm bore of a repurposed Oxford 400 MHz (9.4-T) NMR superconducting magnet. A cylindrical ceramic fiber heater, measuring 2 in. (c.5 cm) in diameter and with a 0.5-in. (c.1.3-cm) inner diameter bore, was affixed inside the cooling jacket within the homogeneous field region of the magnet. This design achieved temperatures up to 1200°C. The ORNL TMP system uses an induction heater, a 2-inch (c.5-cm) diameter water-cooled 0.25-inch (c.0.64-cm) copper tubing wound 10 turns, which is situated within the homogeneous magnetic field region of a 5-in. (c.12.7-cm) diameter, vertical warm-bore 9-T superconducting magnet (American Magnetics, USA). For this study, a susceptor with an inner diameter of 15 mm, a wall thickness of 6 mm, and a length of 75 mm was used to eliminate the effects of induction heating. Schematics of the UF and ORNL TMP systems are shown in Fig. 1a and b, respectively.

The UF TMP system was used to conduct no-field and in-field heat treatments at magnetic field strengths of 0-T, 2-T, 5-T, and 9-T with the cylindrical specimens, while the rectangular specimens were heat-treated at 0-T and 9-T using the ORNL TMP system.

## Sample Preparation

Martensite and pearlite microstructures were formed using different experimental set-ups and heating profiles. For martensite, the cylindrical specimens were encapsulated in quartz tubing [3 in. (c.7.6 cm) long] with a small vent hole made to assist quenching. The encapsulated specimens were placed in the UF TMP system, which maintained the desired magnetic field strength throughout the heat treatment. They were heated at 20°C/min from room temperature to 850°C, followed by a 120-min anneal to achieve sufficient austenitization. The specimens were then ejected from the UF TMP system using a quartz rod and immediately quenched in water. For pearlite, the rectangular specimens were first encapsulated in a quartz tube

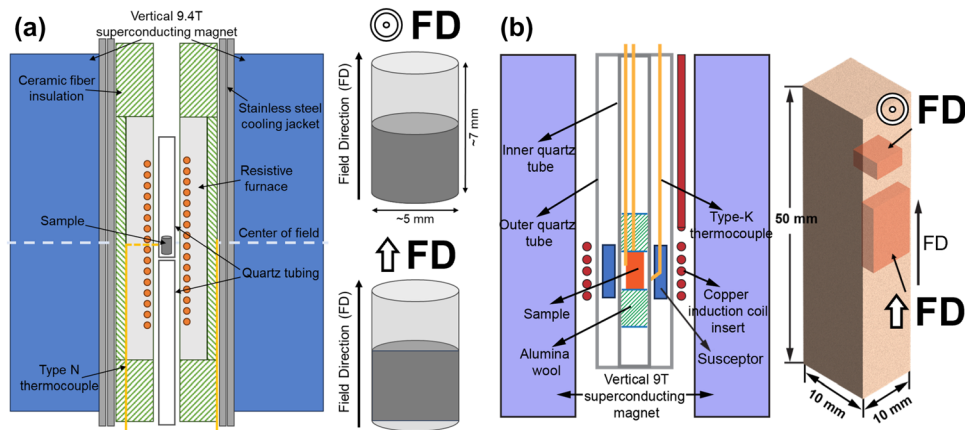


Fig. 1. Schematics of (a) UF High BxT and (b) ORNL TMP systems used for no-field and in-field heat treatment of steel specimens, which were sectioned perpendicular and parallel to the magnetic field direction.

under ultra-high-purity argon gas before being placed in the ORNL TMP system, which is described in detail by Kesler et al.<sup>32</sup> The encapsulated specimens were heated at a rate of 25°C/min from room temperature to 1000°C, then annealed at that temperature for 120 min. After annealing, the specimens were cooled at 50°C/min to 650°C and held at that temperature for approximately 17 min before being furnace-cooled.

All the specimens were cross-sectioned both parallel and perpendicular to the magnetic field direction, as shown in Fig. 1. For the cylindrical martensite specimens, the samples were progressively ground up to 1200-grit SiC paper, followed by hand polishing with 9-, 6-, and 1- $\mu$ m diamond suspensions. Methanol was used after each grinding and polishing step to remove any residual media. Hardness measurements were conducted using a Vickers microhardness indenter with an applied force of 1 kgf, confirming the formation of martensite microstructures with average values between 890 and 950 HV. The grinding and polishing steps were repeated as needed to eliminate surface damage incurred from the hardness measurements. Lastly, to ensure that the sample surfaces were of EBSD quality, a final polishing step was carried out using a vibratory polisher with a 0.05- $\mu$ m non-colloidal silica suspension for 2–4 h.

Similarly, the rectangular pearlite specimens were progressively polished from 240-grit to 1200-grit SiC paper, followed by further polishing with 6- and 1- $\mu$ m diamond suspensions. For EBSD analysis, these samples underwent additional polishing with a vibratory polisher using a 0.02- $\mu$ m colloidal silica suspension for 6 h. The polished samples were then etched with 5% nital for 10 s to reveal the pearlite microstructural features and secondary scanning electron microscope (SEM; Quanta 600; FEI) images were collected.

## Material Characterization

A FEI Helios 5 UC equipped with an EDAX Velocity EBSD CMOS camera was used to collect large-area EBSD scans of the pearlite microstructures. The beam parameters were set to 30 kV and 13 nA, with a step size of 0.5  $\mu$ m, to collect the EBSD data over an area approximately 1 mm by 1 mm, which were analyzed using the TSL 3D OIM software. Additionally, SEM and a Zeiss Axio optical microscope (OM) were used to collect microstructural images from the etched surfaces of the pearlite samples.

EBSD data of the martensite microstructures were obtained using a FEI Helios G4 PFIB equipped with an EDAX Velocity EBSD CMOS camera, where beam parameters of 15 kV and 13 nA, and a step size of 0.2  $\mu$ m were used. Hundreds of martensite EBSD scans at  $\times 10,000$  magnification (a 40.5- $\mu$ m by 32.6- $\mu$ m area) were assembled without over-sampling using montage mapping to form a single EBSD dataset approximately 1 mm by 1 mm. The collected martensite EBSD datasets were processed using the MTEX 5.10.2 open-source toolbox for MATLAB.<sup>33</sup>

Additionally, both thermal etching and chemical etching using picric-based etchants were independently employed in an attempt reveal the prior austenite grain boundaries. Thermal etching was unsuccessful because the cooling rates achievable while maintaining vacuum were insufficient. Chemical etching was unsuccessful because of the low concentration of non-carbon alloying elements in the specimens. As a result, the prior austenite grain sizes and morphologies were determined via parent grain reconstruction using EBSD data.

## Parent Grain Reconstruction

Multiple noise removal steps were performed on the collected martensite EBSD to account for surface defects and to reduce poorly indexed data points. This involved first removing points with an



image quality less than 0.15 times the maximum observed value within the scanned region, and then identifying and removing points that lacked sufficient neighboring interactions to calculate kernel average misorientation. The removed points were not replaced. To avoid exceeding the memory capabilities of MATLAB, the collected EBSD scans were sectioned into equally sized quarters. Consequently, the identified martensite grains (calculated using a  $2^\circ$  threshold) located at the boundaries of these sections, as well as those in regions where scan quality was poor, were excluded from grain analysis to prevent skewed results.

The prior austenite microstructures were reconstructed from the martensite EBSD data using the variant graph approach for parent grain reconstruction developed by Niessen et al.<sup>31,34</sup> A precise orientation relationship (OR) for austenite reconstruction was established based on known martensite–austenite ORs. The Greninger–Troiano orientation relationship was identified as the best match with the smallest mean angular deviation from the experimental data, and was therefore assigned as the starting OR. Threshold values for merging reconstructed austenite grains with similar orientations and inclusions were optimized to ensure the best match between the child martensite orientations and the reconstructed parent grains. With reconstruction having to be performed on quartered EBSD data, the reconstructed parent EBSD data were reassembled before the final calculation of the parent austenite grains. To ensure accuracy, austenite grains located along the boundaries of the EBSD data were excluded from the analysis. The parent austenite grain morphology (including equivalent diameter and aspect ratio) was evaluated using MTEX's built-in shape parameter functions.

Features from the ORTools functional library<sup>31,34</sup> were integrated into the reconstruction process to enhance the analysis of the martensite microstructure, allowing for the measurement of martensite lath/block widths and area fractions of martensite variants. The authors note that, while individual martensite laths are unlikely to be well-resolved under the present EBSD conditions, the lath/block phrasing convention is adopted because it is preferred by the authors of ORTools.

## RESULTS

The prior austenite structure and the resulting pearlite and martensite microstructures are presented in the following sections.

### Prior Austenite Microstructure

To evaluate the austenite microstructure present during heat treatment under varying magnetic field strengths, parent grain reconstruction was performed (as detailed in Sect. “Parent Grain

Reconstruction”) on the collected martensite EBSD data. From the multiple martensite EBSD scans acquired at each magnetic field strength, approximately 275 whole austenite grains were identified in samples oriented perpendicular to the field direction, while about 150 grains were identified in those oriented parallel to the field direction. Figure 2 shows representative inverse pole figure (IPF) maps of the reconstructed parent austenite microstructures for the investigated magnetic field strengths, oriented perpendicular and parallel to the field direction. Parent austenite grain boundaries are marked by bold black lines while annealing twin boundaries are indicated by white lines. Notably, annealing twins were merged before analyzing the parent austenite grain morphology, such that twin boundaries were excluded when calculating grain size.

In this study, one-way analysis of variance (ANOVA) was used to determine whether there were statistically significant differences in grain-

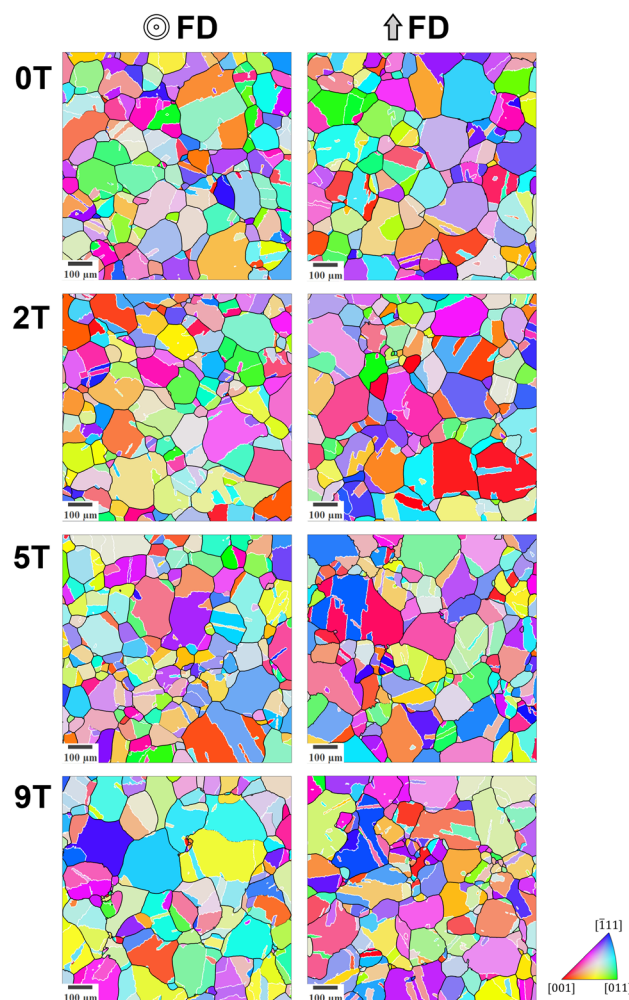


Fig. 2. Inverse pole figure maps of reconstructed parent austenite microstructures from samples heat-treated under varying magnetic field strengths, sectioned both perpendicular and parallel to the field direction; bold black lines indicated parent austenite grains, while annealing twin boundaries are depicted with white lines.

based distributions across the varying magnetic field strengths. The results are presented using standard ANOVA notation, exhibited by  $F(3, 1115) = 1.85, p = 0.137$ . In this notation, the  $F$  statistic ( $F(3, 1115) = 1.85$ ) denotes the ratio of variance between the different magnetic fields to the variance within each group of grains at a given field strength. The numbers in parentheses indicate the degrees of freedom: the first value (3) relates to the magnetic field strengths, while the second value (1115) refers to the number of grains. The  $p$  value ( $p = 0.137$ ) quantifies the probability of observing an  $F$  statistic at least as extreme as the calculated value, assuming the null hypothesis is true. A  $p$  value exceeding 0.05 suggests that there is insufficient evidence to reject the null hypothesis, indicating no statistically significant difference across the varying magnetic field strengths. If the  $p$  value is less than 0.05, a post hoc test—in this case, Tukey's honestly significant difference procedure—is performed to determine which of the groups differ significantly from one another.

The size of the austenite grains remained relatively consistent across the different magnetic field strengths in both field directions, as illustrated in Fig. 3a and b. In this instance, grain size is expressed as equivalent diameter, calculated as twice the measured equivalent radius of each grain. One-way ANOVA revealed no statistically significant difference ( $F(3, 1115) = 1.85, p = 0.137$ ) in grain size for those perpendicular to the magnetic field direction. For austenite grains parallel to the field direction, the difference between the 0-T and the 9-T condition is statistically significant ( $F(3, 605) = 5.23, p = 0.0014$ ), with the 9-T grains having a finer grain size. However, the authors note that, due to the experimental challenge of characterizing large prior austenite grains via EBSD, a relatively small sample of grains was analyzed. It is possible that this result would change if a larger sample of grains was measured.

Beyond size, the shape of the austenite grains is largely unaffected by increasing magnetic field strength. Figure 3c and d shows the aspect ratio of the austenite grains at each magnetic field strength

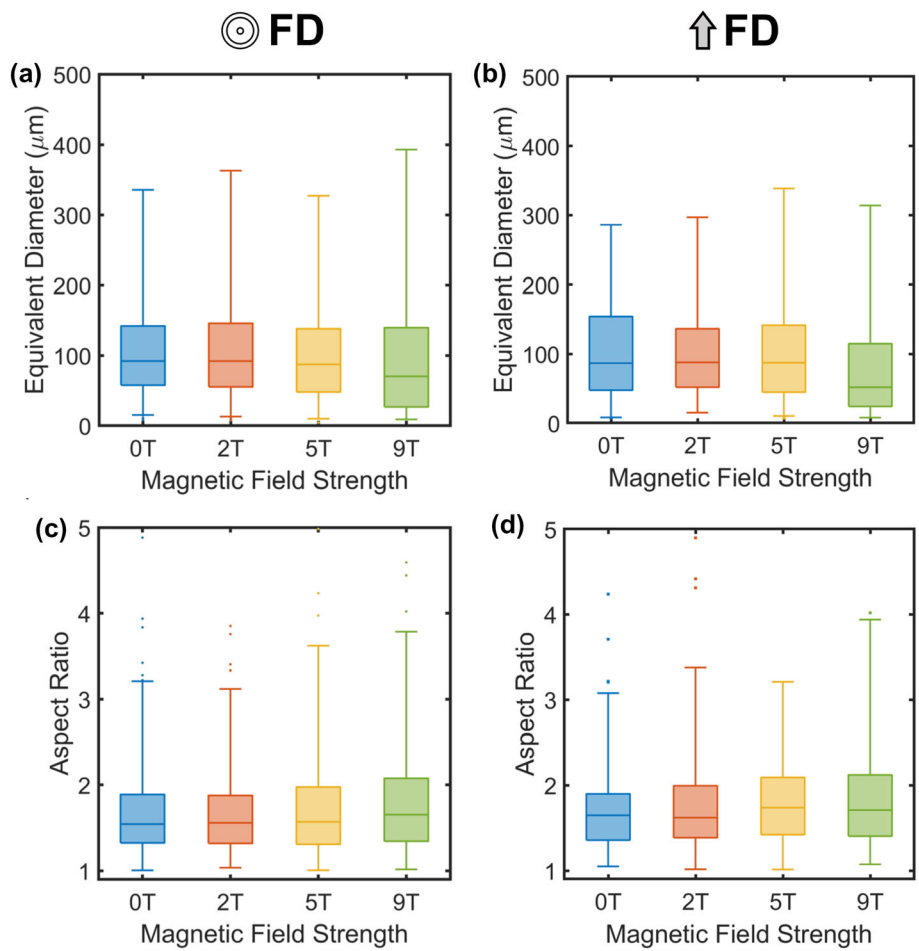


Fig. 3. Equivalent diameter (a, b) and aspect ratio (c, d) of reconstructed parent austenite grains at various magnetic field strengths, oriented perpendicular (a, c) and parallel (b, d) to the field direction. Note that, for the equivalent diameters, the criterion for outliers was calculated after taking a logarithmic transformation of the data to better reflect the natural shape of a grain size distribution.

perpendicular and parallel to the field direction, respectively. Aspect ratio was determined by dividing the long axis of each grain by their short axis. No statistically significant differences in the means are observed perpendicular to ( $F(3, 1115) = 0.85, p = 0.468$ ) or parallel to ( $F(3, 605) = 0.24, p = 0.872$ ) the field direction. There is no evidence of the austenite grains elongation with the magnetic field direction. The crystallographic texture of the parent austenite grains was examined, but no preferential alignment relative to the magnetic field direction was observed.

Differences in annealing twin frequency and morphology were noted and characterized between the different field strengths. To assess the effect of magnetic field strength on annealing twin formation, two twin frequency metrics were used: (1) twin boundary density, ( $N_L$ ), defined as the number of twin boundaries intercepted by a line of length,  $L$ , and (2) the ratio of twin boundary length to grain boundary length. In this study, only twin bound-

aries with a misorientation within a  $3^\circ$  threshold of  $60^\circ$  about  $\langle 111 \rangle$  were identified and analyzed.

Figure 4a shows the variation in twin boundary density across the different magnetic field strengths, perpendicular to the magnetic field direction. These twin boundary density distributions were determined by repeatedly measuring the average twin boundary density along 100 randomly drawn lines within each investigated region. Although the median twin boundary density initially increases with magnetic field strength, it decreases for the 9-T heat-treated sample, falling below that of the 0-T heat-treated sample. One-way ANOVA reveals that there is a statistically significant difference ( $F(3, 146) = 5.26, p = 0.0018$ ) between these twin boundary density distributions for the 0-T and 5-T samples, but the difference remains small. However, for the samples oriented parallel to the field direction, the twin density of the specimen heat treated at 9-T is significantly higher than any other field condition

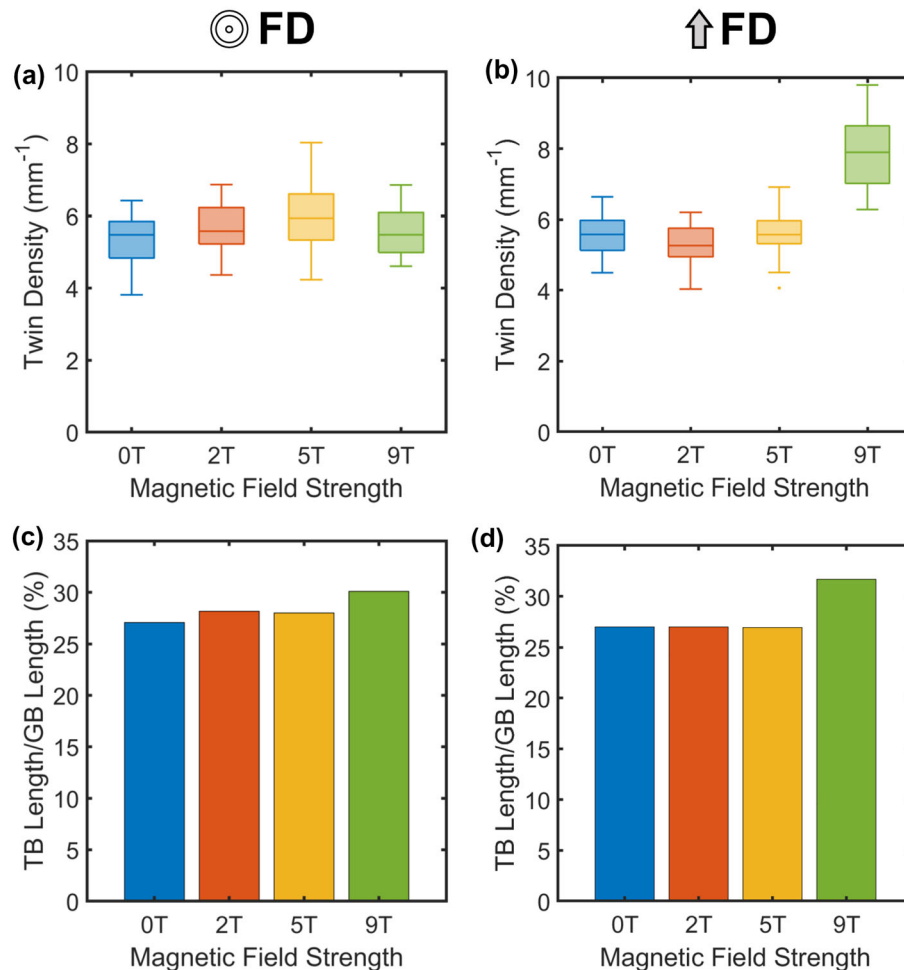


Fig. 4. Annealing twin boundary density ( $N_L$ ) (a, b) and ratio between annealing twin and austenite grain boundaries (c, d) for various magnetic field strengths, oriented perpendicular (a, c) and parallel (b, d) to the field direction.

( $F(3, 75) = 55.39, p = 5.53e^{-19}$ ), as illustrated in Fig. 4b.

Furthermore, the ratio of twin boundary length to grain boundary length for each investigated magnetic field strength is depicted in Fig. 4c and d, perpendicular and parallel to the magnetic field direction, respectively. The ratios displayed represent the average value calculated from various reconstructed areas for each field condition. Perpendicular to the field direction, the boundary length ratio shows a slight increase with increasing magnetic field strength, before experiencing a noticeable jump in the case of the 9-T heat-treated sample. Similarly, parallel to the field direction, while there is no difference between the boundary length ratios of the 0-T, 2-T, and 5-T heat-treated samples, there is a significant increase in this ratio for the 9-T heat-treated sample.

## Pearlite Microstructure

### Proeutectoid Ferrite

To evaluate the proeutectoid ferrite phase evolution, 30 optical microstructural images of the etched pearlite steel samples, oriented perpendicular and parallel to the field, were collected and analyzed for the 0-T and 9-T heat-treated samples. Representative optical micrographs are shown in Fig. 5a. The pearlite and proeutectoid ferrite phases in these microstructures were segmented using ilastik and ImageJ software,<sup>35,36</sup> as shown in Fig. 5b. These segmented images were further analyzed to evaluate the phase fraction of the proeutectoid ferrite phase, and the calculated data are plotted as box plots to show the data distribution, as depicted in Fig. 5c. The data distribution plot clearly indicates

an increase in the proeutectoid ferrite area phase fraction in the 9-T samples compared to the 0-T samples, in both the parallel and perpendicular field directions.

From the optical microstructural images, it is observed that all three types of proeutectoid ferrite phase morphologies (allotriomorph, idiomorphic, and Widmanstätten plates) are present. Additionally, it is also observed from the collected microstructures images that the Widmanstätten ferrite plates increased in the 9-T samples compared to the 0-T heat-treated pearlite samples.

### Pearlite Morphology

Figures 6 and 7 show the IPF maps, secondary SEM images, pearlite block size distributions, and distribution of misorientation angles between neighboring pearlite blocks of the 0-T and 9-T heat-treated samples parallel and perpendicular to the field directions, respectively. The pearlite microstructure is characterized by a lamellar structure consisting of cementite and ferrite phases, both in the form of thin lamellae. Pearlite microstructures consist of lamellar substructures where the ferrite phase has the same crystal orientation and maintains a characteristic orientation relationship with respect to cementite phase, defined as pearlite colonies. The collection of these colonies in pearlite microstructure is defined as a pearlite block in this work. The IPF maps in Fig. 6a, d show the ferrite grain orientations, from which it can be seen that the sample contained equiaxed grains without any preferential texture in both the 0-T- and 9-T-treated samples. Comparing the secondary SEM

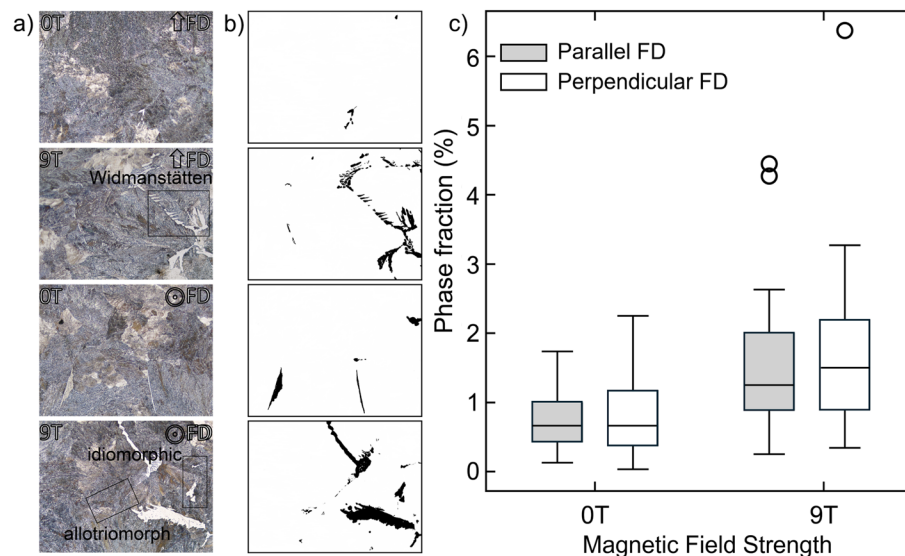


Fig. 5. Proeutectoid ferrite phase fraction calculation: (a) optical micrographs, (b) segmented images, (c) phase fractions with and without field and in each sectioning direction.



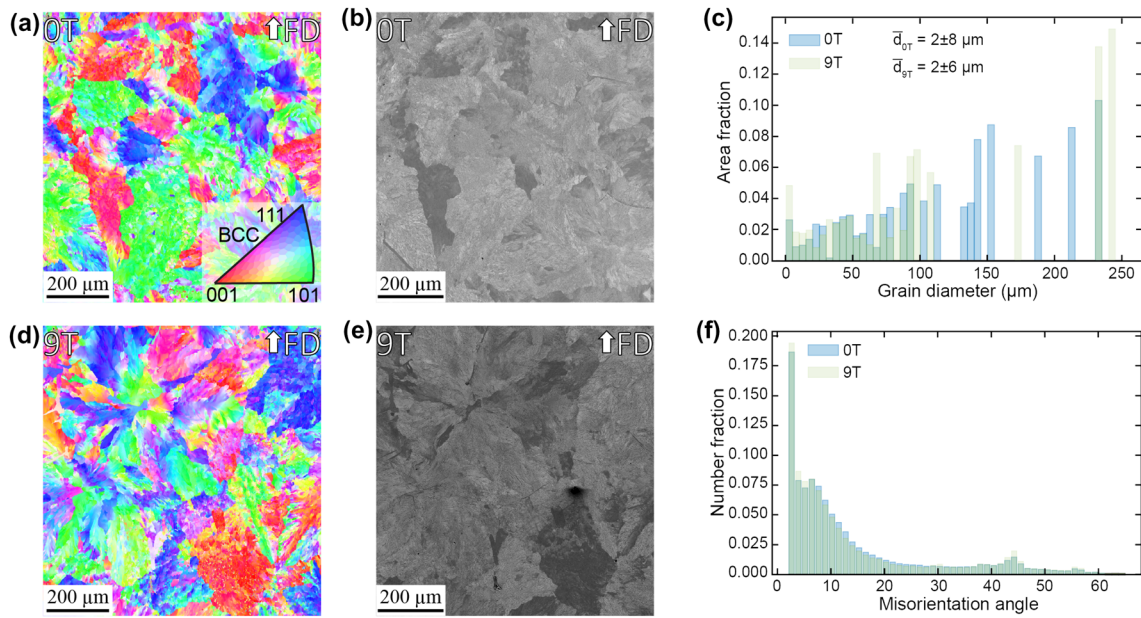


Fig. 6. Pearlite microstructure along field: (a, d) IPF maps referenced to the page normal direction for the 0-T and 9-T specimens, respectively, (b, e) secondary electron images of the same regions after etching, (c) the calculated equivalent pearlite block diameters, (f) the boundary misorientation angles.

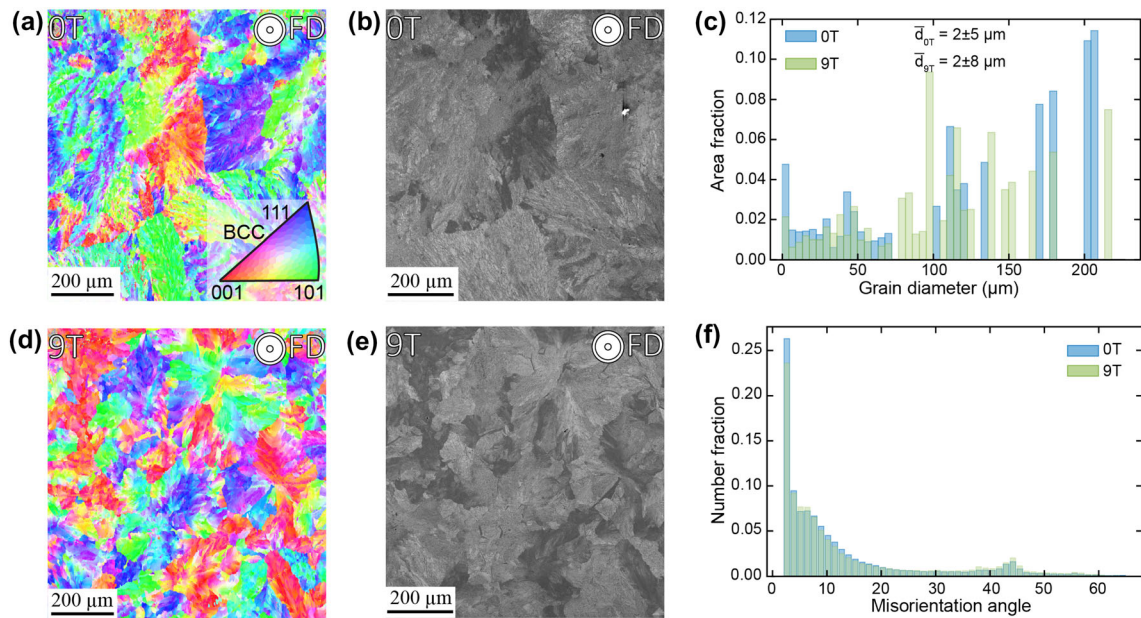


Fig. 7. Pearlite microstructure through field: (a, d) IPF maps referenced to the page normal direction for the 0-T and 9-T specimens, respectively, (b, e) secondary electron images of the same regions after etching, (c) the calculated equivalent pearlite block diameters, (f) the boundary misorientation angles.

micrographs of the same areas of the samples, the pearlite lamellar morphologies of the 0-T and 9-T samples and data show minimal effects due to the magnetic field. Individual, high-resolution images of the SEM micrographs included in Figs. 6 and 7 can be found in Fig. S1 (refer to online supplementary material).

A detailed quantitative analysis of the IPF map was conducted to evaluate microstructural features,

such as pearlite block size and boundary misorientation angle distribution. To measure the pearlite block size from the EBSD map data, we applied a threshold to the ferrite misorientation angle, setting it at  $15^\circ$  or higher.<sup>37,38</sup> The statistics for pearlite block size for both samples are shown in Fig. 6c, from which it can be seen that the mean diameter of the 0-T sample is  $2\ \mu\text{m}$  with a standard deviation of 8, while, for the 9-T pearlite sample, it is  $2\ \mu\text{m}$  with



a standard deviation of 2. Additionally, the boundary misorientation angle distribution has been quantitatively evaluated from the same IPF maps, as shown in Fig. 6f, revealing a high fraction of low-angle grain boundaries in both the 0-T and 9-T heat-treated samples. Similar analyses were conducted on the samples in the direction perpendicular to the field, as shown in Fig. 7. The pearlite block diameters in the perpendicular-to-field direction are comparable to those in the parallel-to-field direction. The boundary misorientation angle distribution is also similar to that of the samples parallel to the field direction, with more pearlite blocks observed in the low-angle boundaries. From these results, it is evident that the magnetic field strength and field direction have a minimal impact on the pearlite block diameters and pearlite orientation distribution.

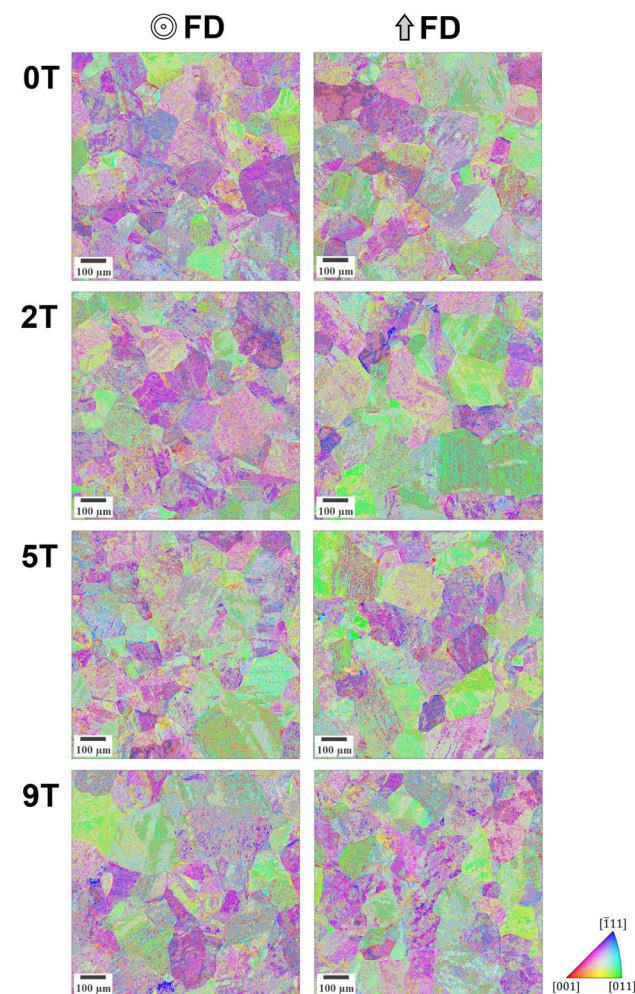


Fig. 8. Inverse pole figure maps of martensite microstructures, collected via montage mapping, from samples heat-treated under varying magnetic field strengths, sectioned both perpendicular and parallel to the field direction.

## Martensite Microstructure

Notably, in this study, the samples were austenitized under a magnetic field, but quenched out of field, which allows the role of the prior austenite structure to be deconvolved from the field effects on the martensite itself.

A representative collection of IPF maps for the martensite microstructures formed after heat treatment under varying magnetic field strengths, oriented perpendicular and parallel to the field directions, is shown in Fig. 8. Regardless of the applied magnetic field strength, a lath morphology was observed, which is expected with the carbon composition of the investigated steel.<sup>39</sup> No elongation or alignment of the martensite laths with the direction of the magnetic field was observed at any field strength.

To further investigate the effect that applying a magnetic field during heat treatment has on the martensite morphology, the lath/block widths of all identified martensite grains were measured. Each collected EBSD scan contains between 500,000 and 800,000 grains, resulting in the analysis of over a million martensite grains for each field condition. The full distribution of lath/block widths, along with a reduced range excluding outliers, is presented in Fig. 9a and b for each investigated magnetic field strength, oriented perpendicular and parallel to the field direction, respectively. The outliers in the lath/block width distributions correspond with the larger, acicular martensite that tended to form along parent austenite grain boundaries and annealing twin boundaries, as illustrated in Fig. 8. The distribution of these outliers is consistent across the different field strengths in both field directions.

The distribution of lath/block widths remains consistent across the different magnetic field strengths in both orientations. A logarithmic variance-stabilizing transformation was applied to the distribution of martensite lath/block widths. No statistically significant difference in martensite lath/block widths was observed with one-way ANOVA for any of the investigated magnetic field strengths in either the perpendicular ( $F(3, 19996) = 4.962, p = 0.065$ ) or parallel ( $F(3, 19996) = 2.574, p = 0.131$ ) directions.

The orientation of the martensite was also examined to assess whether the presence of a magnetic field during heat treatment influenced the formation of specific variants. The martensite variants were indexed according to the convention established by Sun et al.,<sup>40</sup> from which it follows that there are 24 martensite variants categorized into four groups. Each group is transformed from one of four equivalent  $\{111\}_\gamma$ , referred to as packets. Figure 10 shows the area fraction of the 24 martensite variants, identified at each magnetic field strength, in both field directions. Variants are color-coded by packet groupings, with error bars

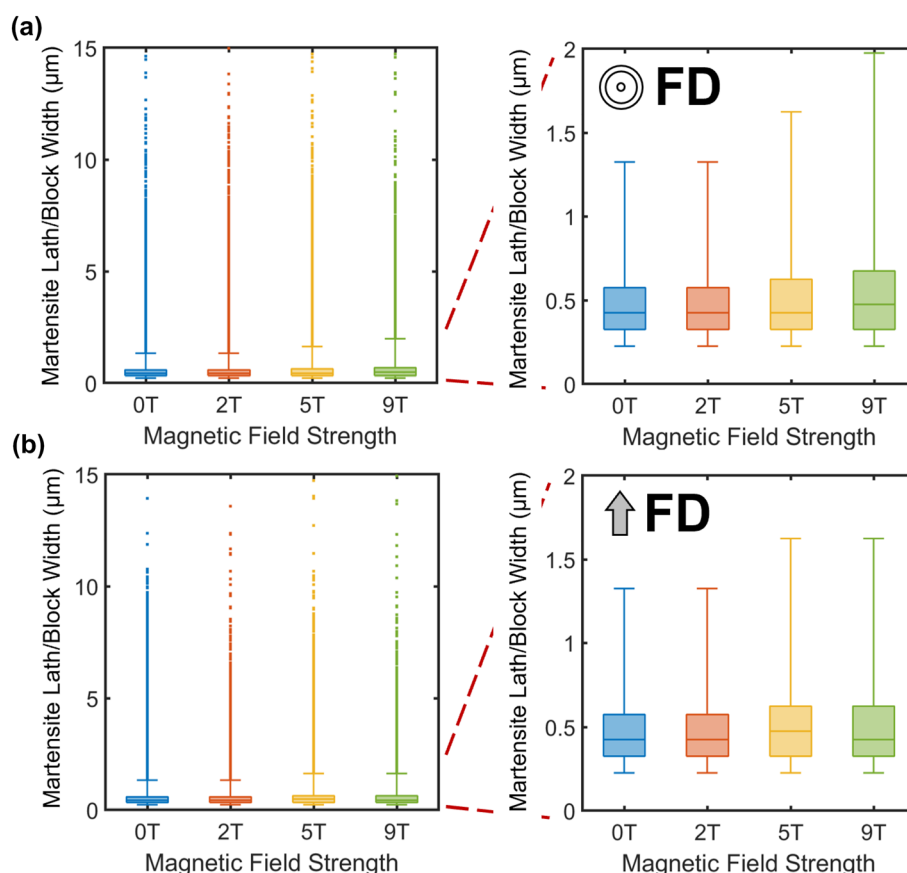


Fig. 9. Distribution of measured martensite lath/block widths for varying magnetic field strengths: (a) perpendicular and (b) parallel to the field direction. As with the grain diameters, the criterion for determining outliers was determined after taking a logarithmic transformation of the distribution to better account for the natural shape of a grain size distribution.

indicating the standard deviation across multiple scans. Overall, the area fraction of each variant remained consistent across different magnetic field strengths and directions, with no significant increase in the presence of specific packets.

## DISCUSSION

In the present study, high-resolution large-area EBSD was used to characterize the microstructures of a near-eutectoid Fe-C alloy heat treated with and without the presence of a high magnetic field. Heat treatments were performed that resulted in pearlitic and martensitic microstructures, and the prior austenite microstructures were reconstructed from the EBSD data. Key field-induced differences were identified and quantified.

### The Role of Magnetic Field on the Prior Austenite Structure

The key observations in the prior austenite structures are a reduction in equivalent grain diameter and in increased annealing twin density at 9-T in comparison to 0-T. Notably, no changes in the austenite grain aspect ratio were observed that would suggest alignment of the grains with the field

direction. Additionally, no evidence of crystallographic alignment of the austenite grains with the field direction was observed.

The observation of a lower grain size in the specimens austenitized under a magnetic field is in contrast to that of Li and Liu,<sup>10</sup> who observed the opposite in a hypereutectoid carbon steel. Specifically, they ran experiments that separated field effects on the pearlite to austenite transformation and field effects on coarsening, finding that the transformation rate was slowed, but the coarsening rate was unaffected. Under their conditions, the limited nucleation during the transformation resulted in a coarser grain size after impingement. The present results are not necessarily incompatible with their observations. For example, it is possible that, in the present experiments, there were a greater number of favorable nucleation sites, so the reduced time for coarsening after the transformation completed under field dominated the final austenite grain size. Additionally, Ref. 10 does not specify the type of heating or the heating/cooling rates, and these key experimental differences likely play a role in austenization behavior. However, further investigation of the balance between

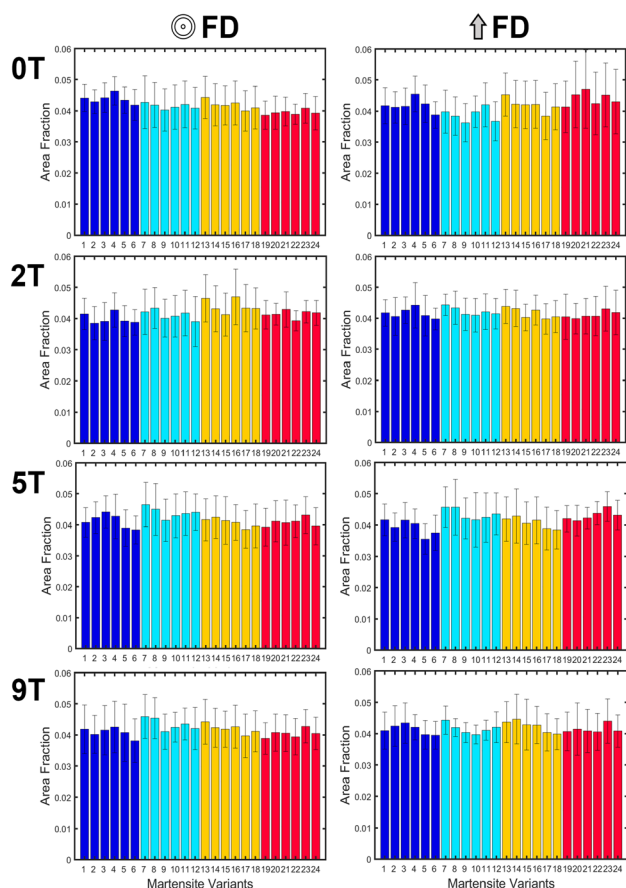


Fig. 10. Area fraction of the 24 martensite variants formed after heat-treatment at varied magnetic field strengths, both perpendicular and parallel to the field direction; variants are color-coded according to their packet groupings.

nucleation and growth under austenitizing conditions is warranted.

Similarly, the observation of no austenite grain alignment with the field is in contrast to another report in the literature. Ohtsuka et al.<sup>25</sup> reported that, when a hypoeutectoid carbon steel with a martensitic microstructure was heated in a field, the resultant austenite grains were aligned with the field direction. However, their samples were also previously deformed via hot rolling. It is possible that the grain morphological alignment may have resulted from aspects of the prior deformation microstructure rather than the applied field, but the effects have not been deconvolved.

Finally, the observation of profuse annealing twins in the prior austenite structure has not been previously observed, likely because some chemical etching methods for revealing prior austenite boundaries are not sensitive to low-energy boundaries such as twins. Some studies of thermal martensites in stainless steels may offer some insights. Shimozono et al.<sup>16</sup> and later Yuan et al.<sup>41</sup> studied the formation of  $\epsilon$  (hcp) martensite under varied levels of magnetic field. Both studies found that the formation of  $\epsilon$  martensite was favored

under high magnetic fields, which the authors suggest results from a decrease in the stacking fault energy under field. Other authors have also suggested changes to stacking fault morphology and apparent energy due to magnetic field effects.<sup>42–44</sup> If a similar effect is present in the Fe-C system, it would explain the presence of increased annealing twins in high magnetic fields.

### Magnetic Field Effects on Pearlite Microstructures

The presence of the magnetic field resulted in two primary effects on the pearlitic microstructures: an increase in proeutectoid ferrite and a transition of that proeutectoid ferrite to increasingly favor a Widmanstätten morphology. No morphological or crystallographic alignment of the proeutectoid ferrite with the field direction was observed.

The increasing fraction of proeutectoid ferrite is consistent with prior reports that the eutectoid invariant reaction is shifted to higher C contents and temperatures with an increased field.<sup>2–5</sup> The resultant increase in proeutectoid ferrite has been observed by other authors,<sup>4,6–8</sup> so it is unsurprising.

However, the lack of alignment of the proeutectoid ferrite is in contrast with the bulk of the literature,<sup>8,20–24</sup> where morphological alignment of the ferrite with the field has been typically reported. As with the elongation of the prior austenite grains, some of these studies used a previously deformed material where the elongation of the grains is both along the field direction along the prior rolling direction, preventing the field effect and deformation effect from being separated.<sup>21,22</sup> However, other studies still reported elongation of the ferrite grains, even in material with a cast starting structure.<sup>8</sup> The majority of these studies were all in significantly hypoeutectoid compositions, with much larger ferrite fractions. In the present near-eutectoid composition, the proeutectoid ferrite morphology may be determined by the austenite grain boundary network rather than by the field direction. Another possible key difference is the cooling rate, as studies with the slowest cooling rates observed the most ferrite elongation,<sup>23,24</sup> while studies with higher cooling rates observed much less alignment.<sup>21</sup> The high cooling rate in the present study, 50°C per minute, may not allow time for growth along the field direction.

The increase in Widmanstätten morphology ferrite at increased magnetic fields is also in contrast to the existing literature. Wang et al. have previously reported a decrease in Widmanstätten ferrite with an increased field.<sup>23,24</sup> The difference may again stem from a difference in composition. As with the ferrite alignment, discussed above, this effect has only been observed in hypoeutectoid steels with a much higher ferrite phase fraction. Alternatively, the slower cooling rate in the studies from the



literature may have allowed the blockier ferrite morphologies to form.

### Magnetic Field Effects on Martensite Microstructures

In this study, samples were austenitized in field, but then quenched out of field to form martensite. This allows the role of the prior austenite structure to be separated from any potential magnetic field effects. As a result, the lack of martensite morphological alignment and preferential variant selection is unsurprising. The most significant difference in the martensite microstructures with increased field is the increasing spread in lath/block widths.

This change in the spread of lath/block widths must result from the prior austenite structure, likely from the finer grain size or the increased density of annealing twins. There are very few studies on the role of annealing twins in martensite nucleation, none in Fe-C, and the existing studies have conflicting results. Tsuzaki et al. considered the martensitic transformation of Fe-32%Ni single and bicrystals during slow cooling and concluded that annealing twins are not particularly potent nucleation sites for martensite.<sup>45</sup> Sadeghi et al. considered the nucleation of athermal  $\alpha'$  martensite in 304 stainless steel and observed that over 97% of observed nucleation sites were at annealing twin boundaries.<sup>46</sup> The role of annealing twins in the formation of martensitic microstructures—with or without a magnetic field—merits greater study.

### CONCLUSION

This work has investigated the role of a high magnetic field during heat treatment in the microstructural evolution of a steel having near-eutectoid composition. Specimens were heated and held above the austenization temperature, then either quenched or cooled to a lower temperature and held to form pearlite. The resulting pearlitic and martensitic microstructures were considered, as was the reconstructed prior austenite structure. The key findings are summarized as follows:

1. Contrary to previous investigations, a finer austenite grain size was observed at the highest 9-T magnetic field strengths relative to the weaker field conditions, although the authors note that this conclusion could be altered with a larger austenite grain sample size. No change was observed in the austenite grain aspect ratio with field strength, but increasing field strength did result in a greater density of annealing twins.
2. The predominantly pearlitic microstructures formed in field showed a statistically meaningful increase in proeutectoid ferrite fraction, but the pearlite did not exhibit any notable texture or boundary texture.
3. The specimens were quenched out of field, so no

morphological alignment or variant selection were observed in the martensitic microstructures. However, specimens austenitized at higher fields exhibited an increased spread in lath/block widths, although the average width did not change significantly.

There are a number of unexplained contradictions between the present study and the general trends in the literature, although there were also key differences in the experimental methodologies. Overall, it is clear that magnetic field-assisted processing, while promising, requires substantial further study.

### SUPPLEMENTARY INFORMATION

The online version contains supplementary material available at <https://doi.org/10.1007/s11837-025-07240-2>.

### ACKNOWLEDGEMENTS

This work is supported by the U.S. Department of Energy's Office of Energy Efficiency and Renewable Energy (EERE) under the Industrial Efficiency & Decarbonization Office (IEDO) award number DE-EE0009131. The views expressed herein do not necessarily represent the views of the U.S. Department of Energy of the United States Government or any agency thereof. The initial construction of the TMP system and the associated facility at the University of Florida were supported by the National High Magnetic Field Laboratory (NHMFL or MagLab) funded by National Science Foundation (NSF) cooperative agreement DMR-1644779 and the State of Florida. The authors would like to express their gratitude to Michael Bates and Jared Lee for their essential role in constructing of the TMP system at the University of Florida. The authors would also like to thank Zhongwei Li and Ramon Padin-Monroig for their assistance with sample fabrication and UF TMP system operations. Finally, the authors acknowledge the use of the Major Analytical Instrumentation Center (MAIC) and Nanoscale Research Facility (NRF) at the University of Florida.

### CONFLICT OF INTEREST

The authors declare that they have no Conflict of interest.

### REFERENCES

1. D. Weiss, B. Murphy, M.J. Thompson, H.B. Henderson, O. Rios, G.M. Ludtka, A. Perron, and M.S. Kesler. 2021. *Int. J. Metalcast.* 15(1): 49. <https://doi.org/10.1007/s40962-020-00460-z>.



2. J.K. Choi, H. Ohtsuka, Y. Xu, and W.Y. Choo. 2000. *Scripta Mater.* 43(3): 221.
3. H. Joo, S. Kim, N. Shin, and Y. Koo. 2000. *Mater. Lett.* 43(5–6): 225. [https://doi.org/10.1016/S0167-577X\(99\)00263-3](https://doi.org/10.1016/S0167-577X(99)00263-3).
4. G.M. Ludtka, R.A. Jaramillo, R.A. Kisner, D.M. Nicholson, J.B. Wilgen, G. Mackiewicz-Ludtka, and P.N. Kalu. 2004. *Scripta Mater.* 51(2): 171. <https://doi.org/10.1016/j.scriptamat.2004.03.029>.
5. R.A. Jaramillo, G.M. Ludtka, R.A. Kisner, D.M. Nicholson, J.B. Wilgen, G. Mackiewicz, N. Bembridge, and P.N. Kalu. 2005. *Investigation of Phase Transformation Kinetics and Microstructural Evolution in 1045 and 52100 Steel Under Large Magnetic Fields*, vol. 1. Hoboken, New Jersey, USA: Wiley.
6. M. Enomoto, H. Guo, Y. Tazuke, Y.R. Abe, and M. Shimotomai. 2001. *Metall. Mater. Trans. A* 32(3): 445. <https://doi.org/10.1007/s11661-001-0061-6>.
7. Y. Zhang, G. Vincent, N. Dewobroto, L. Germain, X. Zhao, L. Zuo, and C. Esling. 2005. *J. Mater. Sci.* 40(4): 903. <https://doi.org/10.1007/s10853-005-6508-1>.
8. Y. Wu, M.L. Gong, S.Y. Wang, X. Zhao, and L. Zuo. 2011. *Alloy Steel Res. Int.* 82(7): 761.
9. Y. Zhang, C. Esling, M. Gong, G. Vincent, X. Zhao, and L. Zuo. 2006. *Scripta Mater.* 54(11): 1897. <https://doi.org/10.1016/j.scriptamat.2006.02.009>.
10. J. Li and W. Liu. 2014. *J. Mater. Res.* 29(13): 102.
11. R. Fields, C. D. Graham, METALLURGICAL TRANSACTIONS A 7A (1976).
12. T. Kakeshita, T. Saburi, K. Kindo, and S. Endo. 1997. *Jpn. J. Appl. Phys.* 36(12R): 7083. <https://doi.org/10.1143/JJAP.36.7083>.
13. H. Ohtsuka, 2006. *Mater. Sci. Eng. A* 438–440: 136. <https://doi.org/10.1016/j.msea.2006.02.087>.
14. H. Ohtsuka, 2007. *Mater. Trans.* 48(11): 2851. <https://doi.org/10.2320/matertrans.MI200718>.
15. V.M. Schastlivtsev, Y.V. Kaletina, E.A. Fokina, and D.A. Mirzaev. 2016. *Metal Sci. Heat Treat.* 58(5–6): 247–253. <https://doi.org/10.1007/s11041-016-9997-4>.
16. T. Shimozono, Y. Kohno, H. Konishi, K. Shibata, H. Ohtsuka, and H. Wada. 1999. *Mater. Sci. Eng. A* 273: 337.
17. K. Shimizu and T. Kakeshita. 1989. *ISIJ Int.* 29(2): 97. <https://doi.org/10.2355/isijinternational.29.97>.
18. T. Kakeshita, T. Saburi, and K. Shimizu. 1999. *Mater. Sci. Eng. A* 273–275: 21–39. [https://doi.org/10.1016/S0921-5093\(99\)00287-7](https://doi.org/10.1016/S0921-5093(99)00287-7).
19. Z.H.I. Sun, M. Guo, J. Vleugels, O. Van der Biest, and B. Blanpain. 2012. *Curr. Opin. Solid State Mater. Sci.* 16(5): 254. <https://doi.org/10.1016/j.cossms.2012.08.001>.
20. H. Ohtsuka, Y. Xu, and H. Wada. 2000. *Mater. Trans. JIM* 41(8): 907. <https://doi.org/10.2320/matertrans1989.41.907>.
21. Y. Zhang, C. He, X. Zhao, L. Zuo, C. Esling, and J. He. 2004. *J. Magnet. Magnet. Mater.* 284: 287. <https://doi.org/10.1016/j.jmmm.2004.06.048>.
22. Y. Zhang, C. He, X. Zhao, C. Esling, and L. Zuo. 2004. *Adv. Eng. Mater.* 6(5): 310.
23. S.J. Wang, X. Zhao, Y.D. Zhang, L. Zuo, and C. Esling. 2007. *Mater. Trans.* 48(11): 2816. <https://doi.org/10.2320/matertrans.MI200706>.
24. S. Wang, X. Zhao, N. Xiao, and L. Zuo. 2012. *J. Mater. Sci. Technol.* 28(6): 552. [https://doi.org/10.1016/S1005-0302\(12\)60096-6](https://doi.org/10.1016/S1005-0302(12)60096-6).
25. H. Ohtsuka, X.J. Hao, and H. Wada. 2003. *Mater. Trans.* 44(12): 2529. <https://doi.org/10.2320/matertrans.44.2529>.
26. Y.D. Zhang, C. Esling, J.S. Lecomte, C.S. He, X. Zhao, and L. Zuo. 2005. *Acta Mater.* 53(19): 5213. <https://doi.org/10.1016/j.actamat.2005.08.007>.
27. T. Kakeshita and T. Fukuda. 2009. *J. Phys. Conf. Ser.* 156(1): 012012. <https://doi.org/10.1088/1742-6596/156/1/012012>.
28. H. Yang and H. Bhadeshia. 2009. *Scripta Mater.* 60(7): 493–495. <https://doi.org/10.1016/j.scriptamat.2008.11.043>.
29. F.B. Pickering and B. Garbarz. 1987. *Scripta Metall.* 21(3): 249–253.
30. A. Brust, E. Payton, T. Hobbs, V. Sinha, V. Yardley, and S. Niezgoda. 2021. *Microsc. Microanal.* 27(5): 1035. <https://doi.org/10.1017/S1431927621012484>.
31. R. Hielscher, T. Nyssönen, F. Niessen, and A. A. Gazder, [arXiv:2201.02103](https://arxiv.org/abs/2201.02103) [cond-mat]ArXiv: 2201.02103 (Jan. 2022).
32. M.S. Kesler, M.A. McGuire, B. Conner, O. Rios, B. Murphy, W. Carter, H.B. Henderson, G.M. Ludtka, and R.A. Kisner. 2021. *J. Thermal Anal. Calor.* 39: 1.
33. F. Bachmann, R. Hielscher, and H. Schaeben. 2010. *Solid State Phenom.* 160: 63.
34. F. Niessen, T. Nyssönen, A.A. Gazder, and R. Hielscher. 2022. *J. Appl. Crystallogr.* 55(1): 180.
35. S. Berg, D. Kutra, T. Kroeger, C.N. Straehle, B.X. Kausler, C. Haubold, M. Schiegg, J. Ales, T. Beier, M. Rudy, K. Eren, J.I. Cervantes, B. Xu, F. Beuttenmueller, A. Wolny, C. Zhang, U. Koethe, F.A. Hamprecht, and A. Kreshuk. 2019. *Nature Methods.* <https://doi.org/10.1038/s41592-019-0582-9>.
36. J. Schindelin, I. Arganda-Carreras, E. Frise, V. Kaynig, M. Longair, T. Pietzsch, S. Preibisch, C. Rueden, S. Saalfeld, B. Schmid, et al. 2012. *Nature Methods* 9(7): 676.
37. N. Guo and Q. Liu. 2012. *J. Microsc.* 246(3): 221.
38. M. Zhou, H. Wang, M. Zhu, J. Tian, X. Su, Q. Zhang, A. Guo, and G. Xu. 2023. *J. Mater. Res. Technol.* 26: 1609.
39. G. Krauss, 1999. *Mater. Sci. Eng. A* 273–275: 40–57. [https://doi.org/10.1016/S0921-5093\(99\)00288-9](https://doi.org/10.1016/S0921-5093(99)00288-9).
40. D. Sun, Z. Guo, and J. Gu. 2021. *Mater. Charact.* 181: 111501. <https://doi.org/10.1016/j.matchar.2021.111501>.
41. J. Yuan, Q. Zhang, J. Wang, L. Wang, C. Wang, and W. Xu. 2022. *Acta Metall. Sin.* 58(12): 1570.
42. F. Bu, Y. Zhang, H. Liu, J. Wang, E. Beaugnon, J. Li, and Y. He. 2023. *J. Mater. Sci. Technol.* 138: 93. <https://doi.org/10.1016/j.jmst.2022.08.014>.
43. L. Vitos, P.A. Korzhavii, J.-O. Nilsson, and B. Johansson. 2008. *Phys. Scripta* 77(6): 065703. <https://doi.org/10.1088/031-8949/77/06/065703>.
44. S. Lu, R. Li, K. Kádas, H. Zhang, Y. Tian, S.K. Kwon, K. Kokko, Q.-M. Hu, S. Hertzman, and L. Vitos. 2017. *Acta Mater.* 122: 72. <https://doi.org/10.1016/j.actamat.2016.09.038>.
45. K. Tsuzaki, N. Harada, and T. Maki. 1995. *Le J. de Phys. IV* 05(C8): C8167. <https://doi.org/10.1051/jp4:1995821>.
46. F. Sadeghi, T. Zargar, J.W. Kim, Y.-U. Heo, J.S. Lee, and C.H. Yim. 2021. *Materialia* 20: 101218. <https://doi.org/10.1016/j.mtla.2021.101218>.

**Publisher's Note** Springer Nature remains neutral with regard to jurisdictional claims in published maps and institutional affiliations.

Springer Nature or its licensor (e.g. a society or other partner) holds exclusive rights to this article under a publishing agreement with the author(s) or other rightsholder(s); author self-archiving of the accepted manuscript version of this article is solely governed by the terms of such publishing agreement and applicable law.